THE JOURNAL OF PHYSICAL CHEMISTRY LETTERS
A JOURNAL OF THE AMERICAN CHEMICAL SOCIETY

pubs.acs.org/JPCL

Letter

In Situ High-Pressure Correlated Transportation of Heavy Rare-Earth Perovskite Nickelates as Batch Synthesized within Eutectic Molten Salts at MPa-p_{O_2}

Yuchen Cui,[†] Jingxin Gao,[†] Hongliang Dong,* Ziang Li, Ziyou Zhang, Vei Wang,* Kaiqi Nie, Zhidan Zeng, Yong Jiang, Nuofu Chen, Ho-kwang Mao, and Jikun Chen*

Cite This: *J. Phys. Chem. Lett.* 2024, 15, 7716−7723

Read Online

ACCESS | Metrics & More | Article Recommendations | Supporting Information

ABSTRACT: The multiple magneto-/electrical quantum transitions discovered with *d*-band correlated metastable perovskite oxides, such as rare-earth nickelate ($ReNiO_3$), enable applications in artificial intelligence and multifunctional sensors. Nevertheless, to date such investigation merely focuses on $ReNiO_3$ with light or middle rare-earth composition, while the analogous explorations toward heavy rare-earth (Re_HNiO_3, Re_H after Gd) are impeded by their ineffective material synthesis relying on GPa pressure. Herein, for the first time we synthesized the powder of Re_HNiO_3 in grams/batch with ∼1000 times lower pressure and ∼300 °C lower temperature in comparison to the previous ∼10^1 milligram/batch results, assisted by their eutectic precipitation and heterogeneous growth within alkali-metal halide molten salt at MPa oxygen pressures. Further *in situ* characterizations under high pressures within a diamond anvil cell reveal a distinguishing pressure predominated bad metal transport within the nonequilibrium state of Re_HNiO_3 showing high-pressure sensitivity up to 10 GPa, and the temperature dependences in electrical transportations are effectively frozen.

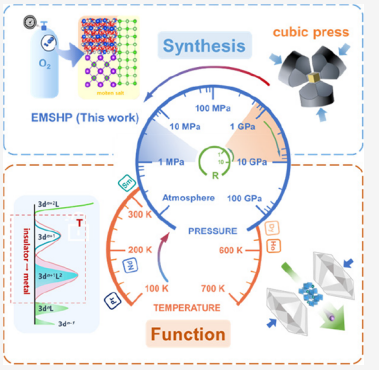

Breaking the thermodynamic restriction and establishing the metastable or unstable electronic phases within electron-correlated semiconductors open up a new paradigm to the exploration of new material functionalities and device applications beyond the conventional.[1] As a representative metastable perovskite, the rare-earth nickelates ($ReNiO_3$) exhibit an extra-ordinarily complex electrical phase diagram and multiple electronic phase transitions, originating from the high tolerance in manipulating its Ni-3d/O-2p orbital configurations via their NiO_6 octahedron.[2−6] The charge disproportionation (antidisproportionation) associated with $Ni^{3+}t_{2g}^6e_g^1 \leftrightarrow Ni^{2+}t_{2g}^6e_g^2$ triggered via critical temperatures (T_{MIT}) enables the metal-to-insulator transition (MIT) of $ReNiO_3$.[3,7] An overwhelming advantage in the MIT functionality of $ReNiO_3$ is the broad adjustability in their T_{MIT} continuously within a wide temperature range of 100−600 K by simply adjusting the composition of *Re*.[8,9] A smaller ionic radius of *Re* distorts the NiO_6 more, which reduces the orbital overlapping between the Ni-3d and O-2p and results in a more stable insulating phase with higher T_{MIT}.[2,4,8,9] Apart from the above band gap regulations, the electronic transportation properties of $ReNiO_3$ can be more directly switched among multiple electronic states via Mottronic orbital filling control.[3,7,10,11] For example, the d-orbital occupancy within $ReNiO_3$ can be increased from $Ni^{3\pm\Delta}t_{2g}^6e_g^{1\pm\Delta}$ (or $Ni^{3+}t_{2g}^6e_g^1$) to $Ni^{2+}t_{2g}^6e_g^2$ via reversable hydrogenation that triggers strong electron localization,[3,7] while a superconductive phase associated with the $Ni^{1+}t_{2g}^6e_g^3$ can be even formed via heavier hydrogenation.[12,13]

These recent discoveries extend the fundamental vision in the field of condensed matter physics and also enrich new electronic applications, such as correlated electronics for artificial intelligence,[14,15] ocean current electric field sensor,[16] correlated electronics for energy conversion,[17] and biosensing.[18]

Nevertheless, the above emerging fundamental discoveries and electronic applications of $ReNiO_3$ were yet limited to light or middle rare-earth composition (e.g., Pr−Gd),[1,2,4,6] while analogous explorations toward heavy rare-earth composition (e.g., Dy−Lu) are impeded by their material synthesis. Unlike the conventional perovskites, the $ReNiO_3$ is in a metastable state and exhibits a positive formation energy ($\Delta G > 0$) that shows an increasing tendency with the atomic number of the rare-earth elements (or reducing ionic radius of *Re*).[19] To date, the synthesis of $ReNiO_3$ with heavy rare-earth composition (Re_HNiO_3) relies on the use of a large volume press that provides extreme conditions, such as 2−6 GPa high pressures and high temperatures beyond 900 °C.[19−22] The necessity of applying such extreme conditions makes the present synthesis

Received: May 22, 2024
Revised: July 3, 2024
Accepted: July 9, 2024
Published: July 23, 2024

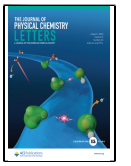

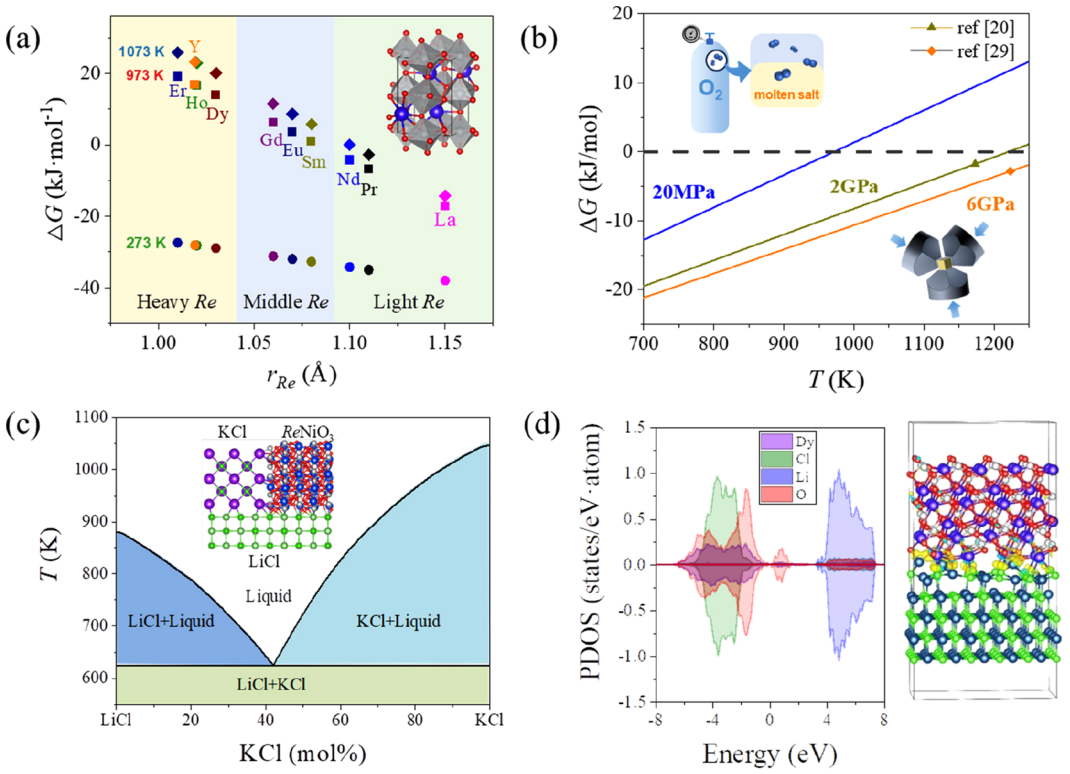

Figure 1. Reducing the positive ΔG of Re_HNiO_3 via molten-salt precipitation. (a) Gibbs free energy of $ReNiO_3$ at three different temperatures, plotted as a function of the radius of different rare metals. (b) Temperature dependence of Gibbs free energy of $ReNiO_3$ with different synthesis conditions. The black dashed line is the boundary between the synthesis requirements of pressure equipment (high-temperature and high-pressure oxygen furnaces and large volume cubic pressure cells, which are shown in the insets). (c) The eutectic phase diagram of the LiCl−KCl melting salt system. The inset shows the side view of the $SmNiO_3(010)$/KCl(001) and $SmNiO_3(101)$/LiCl(001) interface. The purple, green, grayish green, silver, red, and strawberry spheres refer to K, Cl, Li, Ni, O, and Sm atoms, respectively. (d) Partial density of state (PDOS) and charge density difference calculated by density functional theory (DFT). The Fermi energy was taken as the zero-energy reference.

of Re_HNiO_3 with heavy rare-earth composition energy intensive, while their achievable synthesis amounts are rather low. The presently ineffective material synthesize of Re_HNiO_3 with large ΔG in positive magnitudes impedes further exploration of any of their analogous or distinctive electronic applications, compared to $ReNiO_3$ with light or middle rare-earth compositions (Re_LNiO_3 and Re_MNiO_3).[19,23,24]

One distinguishing feature of the Re_HNiO_3 compared to Re_LNiO_3 and Re_MNiO_3 is associated with their more distorted NiO_6 octahedron that further stabilizes the $Ni^{3\pm\Delta}t_{2g}^6e_g^{1\pm\Delta}$ configurations with strongly buckled structure and electronic structure.[3,7] Therefore, potential new electronic structure and correlated transports within Re_HNiO_3 are worthy of exploration via imparting external high pressures that break the thermal equilibrium restrictions to the conventional achievable distortions and/or alignments in their NiO_6 octahedron.[7,20,21,25−28] It is also worth noting that the widened energy band gap (E_g) of Re_HNiO_3 accompanied by their intrinsic lattice shrinkage is driven by the elevated Coulomb repulsions dominated e_g-orbital filling, and this differs from the conventional oxide semiconductors.[3] Nevertheless, the respective impact on the electronic structures upon Re_HNiO_3 via extrinsic lattice shrinkage with pressure is yet an open question to be further explored, and this also relies on a more effective synthesis of Re_HNiO_3.

In this work, for the first time, we achieve the batch synthesis of the powder for the metastable Re_HNiO_3 toward heavy rare-earth composition by developing a eutectic molten salt-assisted heterogeneous precipitation (EMSHP) approach.[22−24] Compared to the large volume press technique, the EMSHP reduces the pressure for synthesizing the powder of $DyNiO_3$, $HoNiO_3$, $YNiO_3$, and $ErNiO_3$ by 200−1000 times (e.g., from 2−6 GPa mechanical pressure to <15 MPa oxygen pressure) and descreases the reaction temperature by 1/3 (e.g., from 950 to 500 °C). This paves the way to explore nonequilibrium electronic phases within the structure and electronic structure of strongly coupled Re_HNiO_3 under GPa magnitude pressures within a diamond anvil cell (DAC). We highlight that the pressure predominated the bad metal transport behaviors of the nonequilibrium Re_HNiO_3, which largely suppresses the temperature dependences in their resistivities, shedding light on potential applications in GPa-pressure sensing.

The positive formation free energy at high magnitudes is the central difficulty that impedes the conventional material synthesis of $ReNiO_3$ with heavy rare-earth composition, as illustrated in Figure 1a. Although the $ReNiO_3$ with light or middle rare-earth composition (e.g., *Re* from Pr to Gd) was more effectively grown via a KCl molten salt-assisted heterogeneous strategy at ∼15 MPa oxygen pressure, it fails in the synthesis of heavy rare-earth $ReNiO_3$ (e.g., *Re* = Dy).[11,23,24] Without the capability to further elevate the bearable oxygen pressure of the reactor, there are two possible routes that further reduce ΔG, as illustrated in Figure 1b: (1) keeping the maximum bearable oxygen pressure but reducing the reaction temperature[20,29] and (2) improving the molten salt-assisted heterogeneous nucleation of $ReNiO_3$.

https://doi.org/10.1021/acs.jpclett.4c01496
J. Phys. Chem. Lett. 2024, 15, 7716−7723

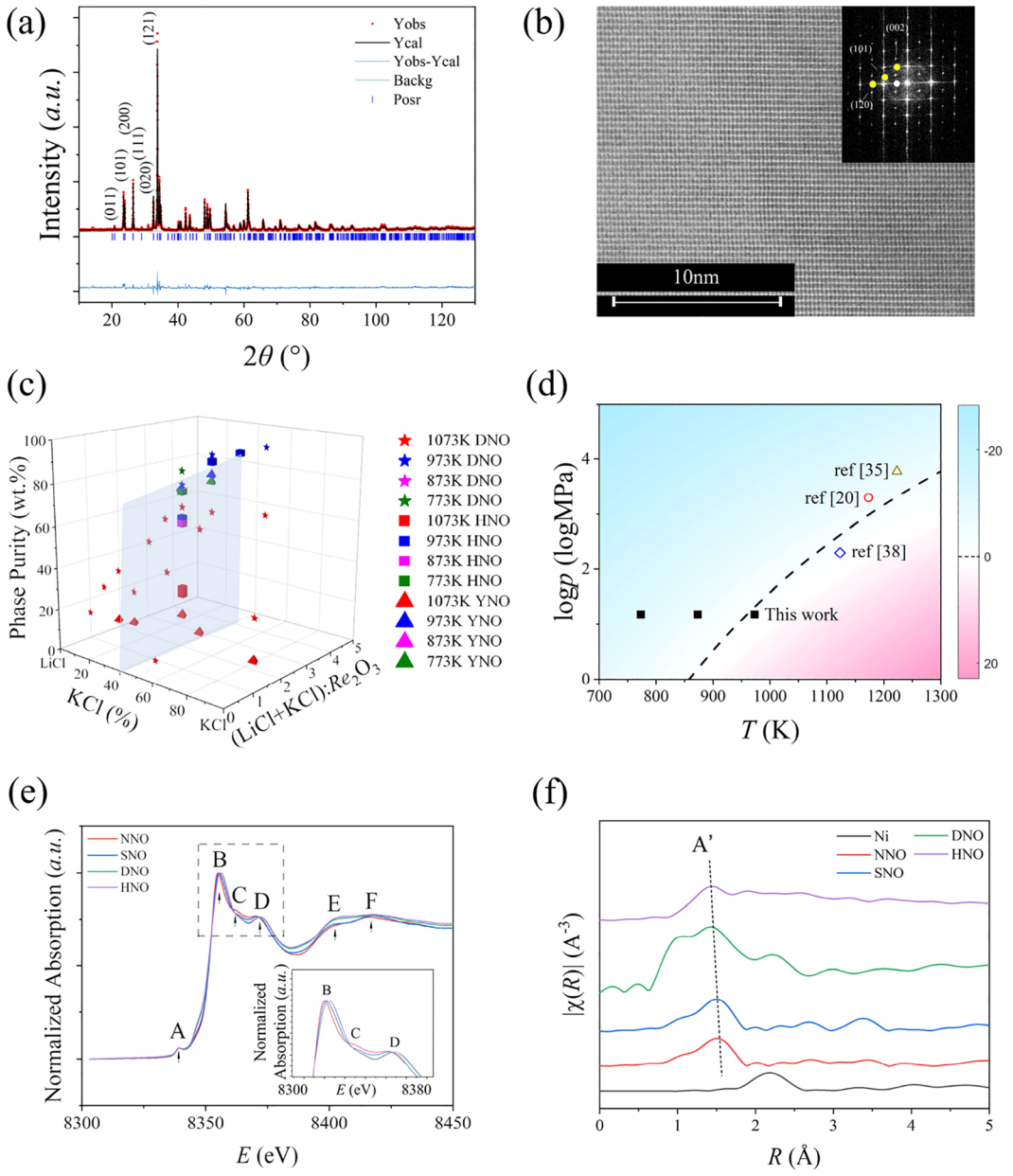

Figure 2. Regulating the structure and electronic structure of Re_HNiO_3. (a) X-ray diffraction patterns and refinements of $DyNiO_3$. (b) Scanning transmission electron microscopy (STEM) image of $HoNiO_3$. The inset shows the electron diffraction pattern of $HoNiO_3$ at different magnifications. (c) Phase purities of $ReNiO_3$ (*Re* = Dy, Ho, Y) in samples obtained under different ratios of molten-salt and preparation conditions. (d) Gibbs energy phase diagram of $DyNiO_3$ with temperature and pressure. Black rectangles represent the result of this work. Green triangle, red circle, and blue diamond represent previous reports. (e) X-ray absorption fine structure (XAFS) of Ni−K edge of $ReNiO_3$ (*Re* = Nd, Sm, Dy, Ho). The inset is an enlarged view of peaks B, C, and D. (f) Fourier transformation (*R*-space) of the Ni−K edge of Ni-foil and $ReNiO_3$ (*Re* = Nd, Sm, Dy, Ho).

Surprisingly, both of the above-proposed strategies can be perfectly realized by simply introducing the eutectic process between KCl and LiCl, as illustrated in Figure 1c. First, mixing KCl and LiCl at their eutectic ratio of 4:6 can effectively reduce the melting point (e.g., 350 °C) compared to KCl (e.g., 774 °C).[30,31] Second, the smaller lattice constant of LiCl (e.g., a = 5.12954 Å) compared to KCl (e.g., a = 6.28400 Å) provides the possibility to trigger the heterogeneous nucleation of $ReNiO_3$ via $ReNiO_3$(101)/LiCl(001), which coordinates the previous heterogeneous nucleation with KCl via $ReNiO_3$(010)/KCl(001). As a result, the required pressure to synthesize Re_HNiO_3 will be reduced from GPa-magnitude mechanical pressure to MPa-magnitude oxygen pressure (i.e., by ∼1000 times), while the reaction temperature can be meanwhile reduced by ∼1/3, as demonstrated in Figure 1b. This sheds light on the possibility of greatly improving the effectiveness of synthesizing Re_HNiO_3 massively without the necessity of using a large volume press. To get insights into the chemical bonding and the stabilizing mechanism of the KCl/LiCl and $ReNiO_3$ interface, herein we take the $DyNiO_3$(010)/KCl(001) system (see Figure 1d) as an example to calculate the partial density of state (PDOS) and charge density difference calculated by using first-principles calculations. From the element-decomposed PDOS (Figure 1d), we can find the hybridization of the O and Li orbitals in the energy region −6 to −2 eV, which clearly indicates the existence of

https://doi.org/10.1021/acs.jpclett.4c01496
J. Phys. Chem. Lett. 2024, 15, 7716−7723

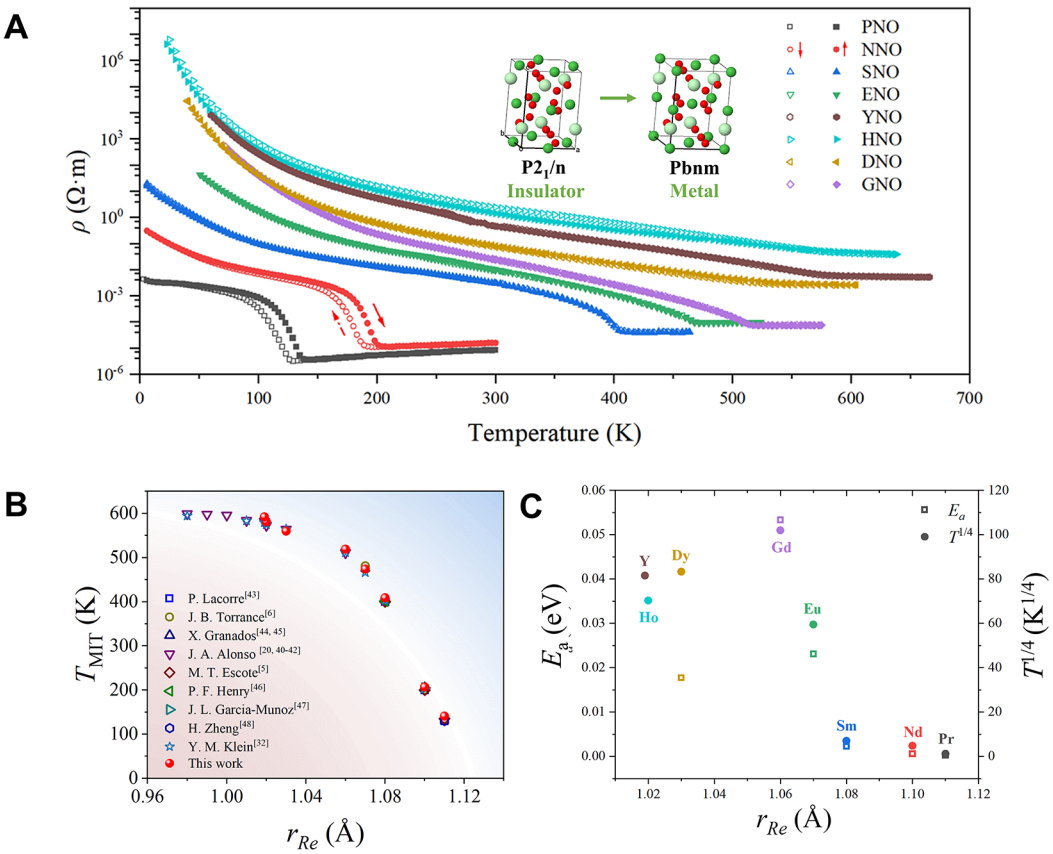

Figure 3. Extending the metal to insulator transition of $ReNiO_3$ toward heavy rare-earth compositions. (a) Resistivity as a function of temperature for $ReNiO_3$ (Re = Pr, Nd, Sm, Eu, Gd, Dy, Ho, Y), where solid circles represent the heating procedure and hollow circles represent the cooling procedure. The inset shows subtle structure change of temperature-driven MIT of $ReNiO_3$ with small ionic radius. (b) Transition temperature (T_{MIT}), (c) Mott temperatures ($T_0^{1/4}$), and activation energies (E_a) of $ReNiO_3$, plotted as the function of the radius of rare metals (r_{Re}).

covalent-like bonding between the polarizations of the polarized PDOS and Li near the interface. Meanwhile, the significant hybridization between O and Dy orbitals in the energy region −5 to −1 eV further stabilizes the system. Typical covalent charge accumulations along the O−Li and O−Dy bonds are observed in the right panel of Figure 1d which verifies our findings. The DFT calculation unveils that the $DyNiO_3(010)/LiCl(001)$ interfacial bonding potentially stabilizes the metastable phase of perovskite $DyNiO_3$ via heterogeneous processes to reduce the previous positive magnitude of formation free energy.

According to the above proposed eutectic molten salt precipitation strategy, we dissolve the percussors of Re_2O_3 and NiO within the mixture of KCl and LiCl under MPa-high oxygen pressures, and afterward coprecipitated the powder of $ReNiO_3$ together with the solidifying KCl and LiCl through heterogeneous nucleation during the cooling down (see Experimental Methods). Figure 2a demonstrates a representative X-ray diffraction (XRD) pattern of as-grown $DyNiO_3$, where the desired perovskite structure is observed with a phase purity >90% as indicated by their structural refinement. As-synthesized powder of $DyNiO_3$ and $HoNiO_3$ exhibits a cubic morphology with size of ∼2 μm, as shown by their scanning electron microscopy (SEM) morphology in Figure S1. The surface orientations of as-grown powder are (001), (101), and (120), as indicated by the scanning transmission electron microscopy (STEM) image shown in Figure 2b. This is in agreement with our expectation about their heterogeneous nucleation via the $Re_HNiO_3(010)/KCl(001)$ and $Re_HNiO_3(101)/LiCl(001)$.

To further confirm the role of eutecticum in the above synthesis, we summarize the phase purity of various heavy rare-earth $ReNiO_3$ (e.g., $DyNiO_3$, $HoNiO_3$, and $YNiO_3$) as synthesized under different conditions, such as the ratio of KCl/LiCl, the ratio of $(KCl+LiCl)/Re_2O_3$, and the reaction temperature, at 15 MPa oxygen pressure. Figures S2, S3, and S4 show the XRD patterns of the $DyNiO_3$, $HoNiO_3$, and $YNiO_3$, respectively, as synthesized under various conditions, while Tables S1, S2, and S3 demonstrate their respective synthesis conditions and more details of the refinements. The accordingly calculated phase purity of as-synthesized Re_HNiO_3 (Re_H = Dy, Y, and Ho) are summarized in Figure 2c. It can be seen that the highest purities are observed for the synthesis using a eutectic molten salt (e.g., KCl:LiCl = 4:6, as marked in blue) at a relatively low reaction temperature (e.g., 600−700 °C).

In Figure 2d, the presently applied oxygen pressures and temperature for the synthesis of $DyNiO_3$ are summarized in the thermodynamic phase stability diagram and also compared to the previous reports.[20,29,32] The dashed line represents the relationship between oxygen pressure and temperature in the case for $\Delta G = 0$, while the blue and pink regions represent the situation where $\Delta G < 0$ and $\Delta G > 0$, respectively. It is also worth noting that the required oxygen pressure to synthesize Re_HNiO_3 is reduced by nearly 3 orders of magnitude compared

https://doi.org/10.1021/acs.jpclett.4c01496
J. Phys. Chem. Lett. 2024, 15, 7716−7723

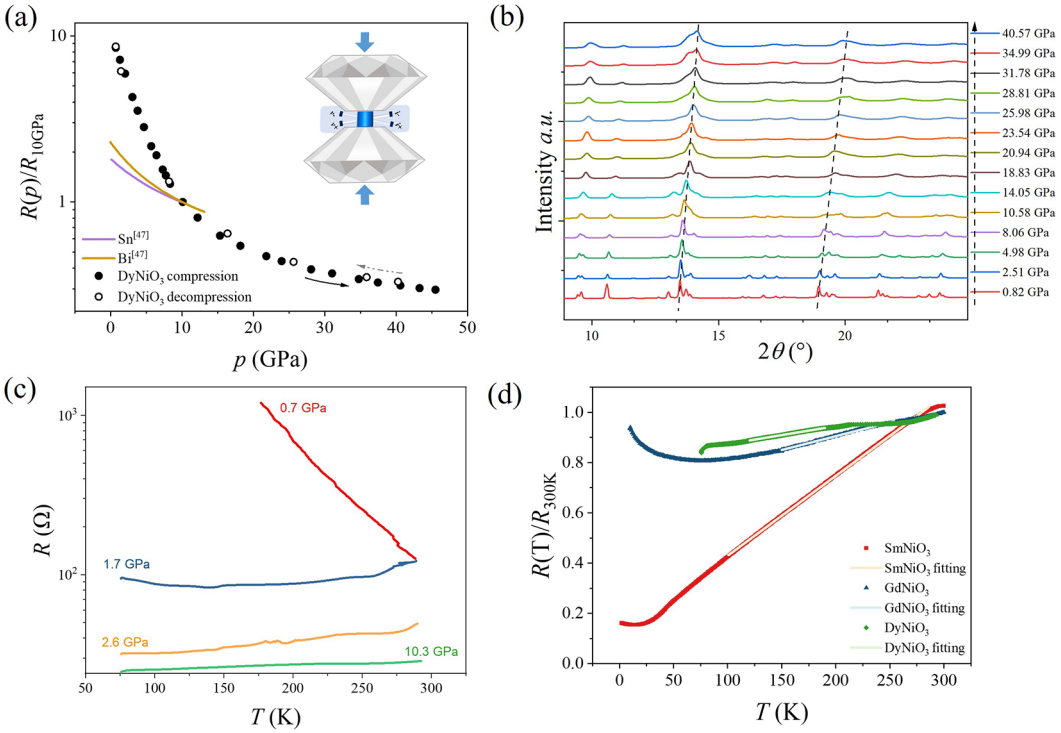

Figure 4. High-pressure regulations in structure and transportations of Re_HNiO_3. (a) Relative resistance ($R(p)/R_{10GPa}$) as a function of pressure measured for $DyNiO_3$, where solid circles represent the compression procedure and hollow circles represent the decompression procedure. The solid lines represent Sn and Pb for comparison. The inset is a schematic diagram of the diamond anvil cell. (b) *In situ* synchrotron-based X-ray diffraction patterns for $DyNiO_3$ from 0.82 to 40.57 GPa. (c) Resistance a function of temperature for $DyNiO_3$ with different pressure. (d) Resistance a function of temperature for $ReNiO_3$ (*Re* = Sm, Gd, Dy) under 10 GPa.

to previous reports,[20,29,32] while the synthesizing temperature is decreased by 400 °C.

To probe the variation in the electronic structure of $ReNiO_3$ versus the rare-earth compositions, we performed X-ray absorption fine structure (XAFS) measurements at beamline BL14W1 station in Shanghai Synchrotron Radiation Facility (SSRF) to probe the Ni−K edge of $ReNiO_3$ with various rare-earth compositions, as shown in Figure 2e. The XAFS spectrum of the Ni−K edge exhibits six characteristic absorption peaks as marked by A−F. The peak A is associated with the quadrupolar transition of Ni-1s → Ni-3d or Ni-1s → Ni-3d/O-2p, and the similar height in peak A for all the $ReNiO_3$ samples indicates their low amount of oxygen vacancy.[33] With a reducing atomic number of the rare-earth element, peak B shifts leftwards and the shoulder-like peak C appears, and this is in agreement with previous observations since enlarging the ionic rare-earth radius stabilizes the metallic orbital configurations.[34−36] The *R*-space calculated from the Fourier transformation of the XAFS spectrum shows a regular offset of the first peak A′ around R = 1.4 Å from $NdNiO_3$ to $HoNiO_3$ in Figure 2f. This peak is attributed to the scattering mode along the Ni−O(1) single path from shell fitting of XAFS[37] (Figure S5), and the reduction of $R_{A'}$ indicates shorter length of Ni−O(1) bonds and more distortion with smaller rare-earth radii.

To characterize their metal-to-insulator transportation behaviors across T_{MIT}, as-grown powders of Re_HNiO_3 were sintered into bulk pellets under a high oxygen pressure of 15 MPa at 700 °C. Figure 3a shows their resistivity measured as a function of temperature ($\rho-T$) that are plotted together with the light and middle rare-earth $ReNiO_3$ as made herein by using the similar molten salt-assisted heterogeneous approach. The rare-earth composition of Tb and Ce are not considered, owing to their variable valence toward +4 and inability to form a stable perovskite structure. The expected discontinuities are clearly observed in the $\rho-T$ of $DyNiO_3$, $HoNiO_3$, and $YNiO_3$ in the high-temperature range of 550−600 K, while their abrupt transitions are smaller compared to those of $ReNiO_3$ with light or middle rare-earth compositions. Their respective T_{MIT} values are more clearly indicated by the temperature dependence of the temperature coefficient of resistance (TCR) as shown in Figure S6 and summarized in Figure 3b as plotted versus the ionic radius of the rare-earth element.[4,6,20,32,38−46] An increasing tendency is observed for T_{MIT} via reduction in the ionic radius of the rare-earth element (or increasing their atomic number), indicating their strengthened insulating phase. This is also reflected from the elevated Mott temperature (T_{Mott}) and activation energy (E_a) for the heavy rare-earth $ReNiO_3$, as calculated from the $\rho-T$ tendency according to the variable range hopping (three-dimensional) model (see more discussion in Figure S7) and thermal activation model, which are shown in Figure 3c.

To further explore their transportation properties under GPa-magnitude pressures, the $ReNiO_3$ samples were pressed into a DAC as illustrated by the inset of Figure 4a. One representative pressure dependence in the resistance ($R-p$) is presented in Figure 4a for $DyNiO_3$ at room temperature, as compared to the ones reported for other typical GPa pressure-sensitive metals such as Sn and Pb.[47] The respective electrical resistance as a function of pressure is demonstrated in Figure S8. This can be ascribed to the decrease in electron−phonon scattering induced by pressure. At a lower pressure range, a

https://doi.org/10.1021/acs.jpclett.4c01496
J. Phys. Chem. Lett. 2024, 15, 7716−7723

much steeper $R-p$ tendency is observed for the $DyNiO_3$. Furthermore, the two-stage behavior in $R-p$ tendency can be observed in various semiconductors, such as Ga_2Te_3 and $Cs_2Au_2Cl_6$,[48] which can be explained by the gradual closure of energy gaps under pressure and less electron−phonon scattering after band overlap.

In Figure 4b, the synchrotron-based X-ray diffraction patterns as measured *in situ* within the DAC are compared for $DyNiO_3$ under various pressures. With the increasing of pressure from 0.82 to 40.57 GPa, the diffraction peaks shift rightward, and this indicates the shrinkage of the lattice constant under high pressures. In addition, it is also worth noting that the symmetries of crystal structures were also elevated via imparting high pressures, as indicated by the merging of several subpeaks.

The $R-T$ tendencies of $DyNiO_3$ under various magnitudes of high pressures are further demonstrated in Figure 4c. The $R-T$ of $DyNiO_3$ shows a semiconductive transportation character at 0.7 GPa, while increasing the pressure toward higher ranges (e.g., above 1.7 GPa) effectively suppresses the temperature dependences in their resistivity. It is also worth noting that at such high-pressure ranges, the transportation character of $DyNiO_3$ also differs from the positive temperature dependence associated with the conventional metals but approaches "bad metals" transport. This is expected to be associated with the strong overlapping between the upper Hubbard Ni-3d band (conductive band) and O-2p (valence band) under GPa high pressures, in which case the carrier scattering will be saturated within the not effectively merged conduction band. Owing to the more distorted NiO_6 octahedron within Re_HNiO_3, it requires higher pressures within the 10^0-10^1 GPa pressure range to completely merge the wider intrinsic E_g associated with the $Ni^{3\pm\Delta}t_{2g}^6e_g^{1\pm\Delta}$ configuration. Therefore, the "bad metal" status with large pressure sensitivity and small temperature dependence can be more effectively preserved within higher range of pressures, shedding a light on potential applications as GPa pressure sensors. This is further demonstrated in Figure 4d, as the positive temperature dependence of $ReNiO_3$ at high pressures is observed to be more effectively suppressed for the ones with a heavier rare-earth composition under 10 GPa. The respective $R-T$ tendencies of $DyNiO_3$, $GdNiO_3$, and $SmNiO_3$ are further fitted by the dual-component model of $\rho = \rho_0 + A_1T + A_2T^2$,[49] where two characteristic parameters, the residual resistivity (ρ_0) and the characteristic temperature (T^*), are summarized in Table S5. In general, reducing the rare-earth radius (or more distorted NiO_6 octahedra) elevates ρ_0 and reduces T^*, and this indicates a transportation behavior more toward correlated metal, while high pressure effectively freezes the electron−electron scattering.[50]

In conclusion, we demonstrate a eutectic molten salt-assisted heterogeneous precipitation approach that for the first time achieves the batch synthesis of $ReNiO_3$ covering the heavy rare-earth compositions (e.g., Re = Dy, Ho, Y). Assisted by the heterogeneous growth of Re_HNiO_3 along with the eutectic precipitation of metal alkali halide molten salt, the synthesizing pressure is effectively reduced from the previous 2−6 GPa to below 10 MPa while the temperature is reduced from the previous 900 to 600 °C. It greatly amplifies the synthesis amount of Re_HNiO_3 from the previous tens of milligrams per batch for using high-pressure synthesis up to tens of grams per batch, which paves the way for their electronic applications. Based on their more electron-localized $Ni^{3\pm\Delta}t_{2g}^6e_g^{1\pm\Delta}$ configuration as probed by the XAFS, a pressure-dependent bad metallicity transport character was discovered in 1.7−10.3 GPa-pressured Re_HNiO_3, showing higher pressure sensitivity compared to the pressure-sensitive metals and low temperature dependence. This is attributed to the strong coupling between the structure and electronic structure of Re_HNiO_3 at $Ni^{3\pm\Delta}t_{2g}^6e_g^{1\pm\Delta}$ configurations, in which case the previous temperature dependence in the electronic structure and its resultant transportation behavior are structurally locked by the imparted GPa range pressures. Such pressure dominance in the electronic structure of the GPa-pressured nonequilibrium Re_HNiO_3 overwhelms their previous temperature dependence, shedding light on potential applications in GPa pressure sensing.

EXPERIMENTAL METHODS

Material Growth. A eutectic molten salt-assisted heterogeneous precipitation (EMSHP) approach was used for synthesizing the powders of representative rare-earth nickelates, such as $HoNiO_3$, $DyNiO_3$, $ErNiO_3$, and $YNiO_3$. The oxide precursors of Re_2O_3 and NiO at nominal stoichiometry were dissolved within LiCl and KCl mixture molten salt at a reaction temperature of 500−800 °C for 12 h under 15 MPa oxygen pressure. Afterward, the melt was slowly cooled to process the powders, which were then rinsed in water under ultrasonic treatment several times to remove the KCl and LiCl. As-obtained powders were further cold pressed into pellets and annealed at the same pressure and temperatures for further characterizations.

Material Characterizations. The Ni−K, Ni−L, and O−K edge of various $ReNiO_3$ samples were characterized by X-ray absorption fine structure (XAFS) at beamline BL14W1 station in Shanghai Synchrotron Radiation Facility (SSRF). The crystal structures were characterized by X-ray diffraction (XRD) and scanning transmission electron microscopy (STEM). The temperature dependence of electronic resistivity within 300−500 K was measured by using a commercial CTA-system within the temperature range from 300 to 550 K in vacuum, while the one within 5−300 K was measured by using a commercial PPMS system from Quantum Design. The high-pressure experiments were performed by using diamond anvil cells (DACs). T301 stainless steel was used as gasket, and a 100 μm center hole was drilled as a sample chamber. Powdered samples were loaded into the sample chamber. A ruby ball was used to determine the pressure. Ruby fluorescence technology was used to calibrate the pressure of all experiments.

ASSOCIATED CONTENT

Data Availability Statement

The data that support the findings of this study are available from the corresponding author upon reasonable request.

Supporting Information

The Supporting Information is available free of charge at https://pubs.acs.org/doi/10.1021/acs.jpclett.4c01496.

Details of calculation of Gibbs free energy and the First Principle study, additional SEM morphology, more XRD patterns and refinements, and details of ρ-T model (PDF)

https://doi.org/10.1021/acs.jpclett.4c01496
J. Phys. Chem. Lett. 2024, 15, 7716−7723

AUTHOR INFORMATION

Corresponding Authors

Hongliang Dong − *Center for High Pressure Science and Technology Advanced Research, Shanghai 201203, China; Shanghai Key Laboratory of Material Frontiers Research in Extreme Environments (MFree), Shanghai Advanced Research in Physical Sciences (SHARPS), Shanghai 201203, P.R. China; State Key Laboratory of High Performance Ceramics and Superfine Microstructure, Shanghai Institute of Ceramics, Chinese Academy of Sciences, Shanghai 201899, China*; Email: hongliang.dong@hpstar.ac.cn

Vei Wang − *Department of Applied Physics, Xi'an University of Technology, Xi'an 710054, China*; Email: wangvei@xaut.edu.cn

Jikun Chen − *School of Materials Science and Engineering, University of Science and Technology Beijing, Beijing 100083, China*; orcid.org/0000-0002-0860-5106; Email: jikunchen@ustb.edu.cn

Authors

Yuchen Cui − *School of Materials Science and Engineering, University of Science and Technology Beijing, Beijing 100083, China*

Jingxin Gao − *School of Materials Science and Engineering, University of Science and Technology Beijing, Beijing 100083, China*

Ziang Li − *School of Materials Science and Engineering, University of Science and Technology Beijing, Beijing 100083, China*

Ziyou Zhang − *Center for High Pressure Science and Technology Advanced Research, Shanghai 201203, China*

Kaiqi Nie − *Beijing Synchrotron Radiation Facility, Institute of High Energy Physics, Chinese Academy of Sciences, Beijing 100049, China*

Zhidan Zeng − *Center for High Pressure Science and Technology Advanced Research, Shanghai 201203, China*; orcid.org/0000-0003-4283-2393

Yong Jiang − *School of Materials Science and Engineering, University of Science and Technology Beijing, Beijing 100083, China*; orcid.org/0000-0003-2011-7241

Nuofu Chen − *School of Renewable Energy, North China Electric Power University, Beijing 102206, China*; orcid.org/0000-0002-9584-0699

Ho-kwang Mao − *Center for High Pressure Science and Technology Advanced Research, Shanghai 201203, China; Shanghai Key Laboratory of Material Frontiers Research in Extreme Environments (MFree), Shanghai Advanced Research in Physical Sciences (SHARPS), Shanghai 201203, P.R. China*

Complete contact information is available at: https://pubs.acs.org/10.1021/acs.jpclett.4c01496

Author Contributions

†Yuchen Cui and Jingxin Gao contributed equally to this work.

Notes

The authors declare no competing financial interest.

ACKNOWLEDGMENTS

The authors acknowledge funding support from the National Key Research and Development Program of China (No. 2021YFA0718900). This work was supported by National Natural Science Foundation of China (No. 61674013). In addition, this work was also partly supported by the Opening Project of State Key Laboratory of High Performance Ceramics and Superfine Microstructure (Project No. SKL201802SIC). V. Wang acknowledges financial support from the Scientific Research Program Funded by Shanxi Provincial Education Department (Grant No. 22JP058). We also thank the BL14W1 station in Shanghai Synchrotron Radiation Facility (SSRF) for the help in characterizations. J. Chen also acknowledges the financial support from the Xiaomi scholarship.

REFERENCES

(1) Aykol, M.; Dwaraknath, S. S.; Sun, W.; Persson, K. A. Thermodynamic limit for synthesis of metastable inorganic materials. *Sci. Adv.* **2018**, *4* (4), No. eaaq0148.

(2) Catalan, G. Progress in perovskite nickelate research. *Phase Transit.* **2008**, *81* (7−8), 729−749.

(3) Shi, J.; Zhou, Y.; Ramanathan, S. Colossal resistance switching and band gap modulation in a perovskite nickelate by electron doping. *Nat. Commun.* **2014**, *5* (1), 4860.

(4) Escote, M. T.; da Silva, A. M. L.; Matos, J. R.; Jardim, R. F. General Properties of Polycrystalline $LnNiO_3$ (Ln = Pr, Nd, Sm) Compounds Prepared through Different Precursors. *J. Solid State Chem.* **2000**, *151* (2), 298−307.

(5) Li, H.; Wang, Y.; Meng, F.; Mao, W.; Cao, X.; Bian, Y.; Zhang, H.; Jiang, Y.; Chen, N.; Chen, J. Metal-organic decomposition growth of thin film metastable perovskite nickelates with kinetically improved quantum transitions. *Int. J. Min. Met. Mater.* **2023**, *30* (12), 2441−2450.

(6) Torrance, J. B.; Lacorre, P.; Nazzal, A. I.; Ansaldo, E. J.; Niedermayer, Ch. Systematic study of insulator-metal transitions in perovskites $RNiO_3$ (R = Pr, Nd, Sm, Eu) due to closing of charge-transfer gap. *Phys. Rev. B* **1992**, *45* (14), 8209.

(7) Chen, J.; Li, Z.; Dong, H.; Xu, J.; Wang, V.; Feng, Z.; Chen, Z.; Chen, B.; Chen, N.; Mao, H.-K. Pressure Induced Unstable Electronic States upon Correlated Nickelates Metastable Perovskites as Batch Synthesized via Heterogeneous Nucleation. *Adv. Funct. Mater.* **2020**, *30* (23), 2000987.

(8) Zhang, H.; Bian, Y.; Xia, Y.; Cui, Y.; Li, Z.; Zhang, F.; Bai, Y.; Chen, N.; Chen, J. Correlated perovskite nickelates with valence variable rare-earth compositions. *J. Rare. Earth* **2024**, *42*, 743.

(9) Zhong, J.; Li, Z.; Zheng, Y.; Jiang, P.; Zhang, F.; Zhang, T.; Cui, Y.; Zhong, Z.; Chen, N.; Chen, J. Extending the metal to insulator transitions of rare-earth nickelates towards low temperature ranges. *J. Am. Ceram. Soc.* **2023**, *106* (8), 5067−5077.

(10) Chen, J.; Mao, W.; Gao, L.; Yan, F.; Yajima, T.; Chen, N.; Chen, Z.; Dong, H.; Ge, B.; Zhang, P.; et al. Electron-Doping Mottronics in Strongly Correlated Perovskite. *Adv. Mater.* **2020**, *32* (6), 1905060.

(11) Bian, Y.; Li, H.; Yan, F.; Li, H.; Wang, J.; Zhang, H.; Jiang, Y.; Chen, N.; Chen, J. Hydrogen induced electronic transition within correlated perovskite nickelates with heavy rare-earth composition. *Appl. Phys. Lett.* **2022**, *120* (9), 092103.

(12) Li, D.; Lee, K.; Wang, B. Y.; Osada, M.; Crossley, S.; Lee, H. R.; Cui, Y.; Hikita, Y.; Hwang, H. Y. Superconductivity in an infinite-layer nickelate. *Nature* **2019**, *572* (7771), 624−627.

(13) Shao, T.-N.; Zhang, Z.-T.; Qiao, Y.-J.; Zhao, Q.; Liu, H.-W.; Chen, X.-X.; Jiang, W.-M.; Yao, C.-L.; Chen, X.-Y.; Chen, M.-H.; et al. Kondo scattering in underdoped $Nd_{1-x}Sr_xNiO_2$ infinite-layer superconducting thin films. *Natl. Sci. Rev.* **2023**, *10* (11), No. nwad112.

(14) Zhang, H.-T.; Park, T. J.; Islam, A. N. M. N.; Tran, D. S. J.; Manna, S.; Wang, Q.; Mondal, S.; Yu, H.; Banik, S.; Cheng, S.; et al. Reconfigurable perovskite nickelate electronics for artificial intelligence. *Science* **2022**, *375* (6580), 533−539.

(15) Shi, J.; Ha, S. D.; Zhou, Y.; Schoofs, F.; Ramanathan, S. A correlated nickelate synaptic transistor. *Nat. Commun.* **2013**, *4* (1), 2676.

(16) Zhang, Z.; Schwanz, D.; Narayanan, B.; Kotiuga, M.; Dura, J. A.; Cherukara, M.; Zhou, H.; Freeland, J. W.; Li, J.; Sutarto, R.; et al. Perovskite nickelates as electric-field sensors in salt water. *Nature* **2018**, *553* (7686), 68−72.
(17) Zhou, Y.; Guan, X.; Zhou, H.; Ramadoss, K.; Adam, S.; Liu, H.; Lee, S.; Shi, J.; Tsuchiya, M.; Fong, D. D.; et al. Strongly correlated perovskite fuel cells. *Nature* **2016**, *534* (7606), 231−234.
(18) Sun, Y.; Nguyen, T. N. H.; Anderson, A.; Cheng, X.; Gage, T. E.; Lim, J.; Zhang, Z.; Zhou, H.; Rodolakis, F.; Zhang, Z.; et al. In Vivo Glutamate Sensing inside the Mouse Brain with Perovskite Nickelate−Nafion Heterostructures. *ACS Appl. Mater. Interfaces* **2020**, *12* (22), 24564−24574.
(19) Jaramillo, R.; Schoofs, F.; Ha, S. D.; Ramanathan, S. High pressure synthesis of $SmNiO_3$ thin films and implications for thermodynamics of the nickelates. *Journal of Materials Chemistry C* **2013**, *1* (13), 2455−2462.
(20) Alonso, J. A.; Martínez-Lope, M. J.; Casais, M. T.; Martínez, J. L.; Demazeau, G.; Largeteau, A.; García-Muñoz, J. L.; Muñoz, A.; Fernández-Díaz, M. T. High-Pressure Preparation, Crystal Structure, Magnetic Properties, and Phase Transitions in $GdNiO_3$ and $DyNiO_3$ Perovskites. *Chem. Mater.* **1999**, *11* (9), 2463−2469.
(21) Obradors, X.; Paulius, L. M.; Maple, M. B.; Torrance, J. B.; Nazzal, A. I.; Fontcuberta, J.; Granados, X. Pressure dependence of the metal-insulator transition in the charge-transfer oxides $RNiO_3$ (R = Pr, Nd, $Nd_{0.7}La_{0.3}$). *Phys. Rev. B* **1993**, *47* (18), 12353−12356.
(22) Yan, F.; Mi, Z.; Chen, J.; Hu, H.; Gao, L.; Wang, J.; Chen, N.; Jiang, Y.; Qiao, L.; Chen, J. Revealing the role of interfacial heterogeneous nucleation in the metastable thin film growth of rare-earth nickelate electronic transition materials. *Phys. Chem. Chem. Phys.* **2022**, *24* (16), 9333−9344.
(23) Li, Z.; Yan, F.; Li, X.; Cui, Y.; Wang, V.; Wang, J.; Liu, C.; Jiang, Y.; Chen, N.; Chen, J. Molten-salt synthesis of rare-earth nickelate electronic transition semiconductors at medium high metastability. *Scripta Mater.* **2022**, *207*, 114271.
(24) Chen, J.; Hu, H.; Wang, J.; Yajima, T.; Ge, B.; Ke, X.; Dong, H.; Jiang, Y.; Chen, N. Overcoming synthetic metastabilities and revealing metal-to-insulator transition & thermistor bi-functionalities for d-band correlation perovskite nickelates. *Mater. Horiz.* **2019**, *6* (4), 788−795.
(25) Drozdov, A. P.; Eremets, M. I.; Troyan, I. A.; Ksenofontov, V.; Shylin, S. I. Conventional superconductivity at 203 K at high pressures in the sulfur hydride system. *Nature* **2015**, *525* (7567), 73−76.
(26) Medarde, M.; Mesot, J.; Lacorre, P.; Rosenkranz, S.; Fischer, P.; Gobrecht, K. High-pressure neutron-diffraction study of the metallization process in $PrNiO_3$. *Phys. Rev. B* **1995**, *52* (13), 9248−9258.
(27) Zhou, J. S.; Goodenough, J. B.; Dabrowski, B. Pressure-Induced Non-Fermi-Liquid Behavior of $PrNiO_3$. *Phys. Rev. Lett.* **2005**, *94* (22), 226602.
(28) Drozdov, A. P.; Kong, P. P.; Minkov, V. S.; Besedin, S. P.; Kuzovnikov, M. A.; Mozaffari, S.; Balicas, L.; Balakirev, F. F.; Graf, D. E.; Prakapenka, V. B.; et al. Superconductivity at 250 K in lanthanum hydride under high pressures. *Nature* **2019**, *569* (7757), 528−531.
(29) Demazeau, G.; Marbeuf, A.; Pouchard, M.; Hagenmuller, P. Sur une série de composés oxygènes du nickel trivalent derivés de la perovskite. *J. Solid State Chem.* **1971**, *3* (4), 582−589.
(30) Mao, H.-K.; Chen, X.-J.; Ding, Y.; Li, B.; Wang, L. Solids, liquids, and gases under high pressure. *Rev. Mod. Phys.* **2018**, *90* (1), No. 015007.
(31) Janz, G. J. *Molten Salts Handbook*; Academic Press, 1967.
(32) Klein, Y. M.; Kozłowski, M.; Linden, A.; Lacorre, P.; Medarde, M.; Gawryluk, D. J. *RE*NiO_3 Single Crystals (*RE* = Nd, Sm, Gd, Dy, Y, Ho, Er, Lu) Grown from Molten Salts under 2000 bar of Oxygen Gas Pressure. *Cryst. Growth Des.* **2021**, *21* (7), 4230−4241.
(33) Moriga, T.; Kikkawa, S.; Takahashi, M.; Kanamaru, F.; Nakabayashi, I. XAFS Study on Reduction Process of Pauli-Paramagnetic $LaNiO_3$ to Antiferromagnetic $La_2Ni_2O_5$. *Jpn. J. Appl. Phys.* **1993**, *32* (S2), 764.
(34) Acosta-Alejandro, M.; de León, J. M.; Medarde, M.; Lacorre, P.; Konder, K.; Montano, P. A. Local lattice structure change in $PrNiO_3$ across the metal-insulator transition: X-ray absorption near-edge structure spectroscopy and ab initio calculations. *Phys. Rev. B* **2008**, *77* (8), No. 085107.
(35) Medarde, M.; Fontaine, A.; García-Muñoz, J. L.; Rodríguez-Carvajal, J.; de Santis, M.; Sacchi, M.; Rossi, G.; Lacorre, P. $RNiO_3$ perovskites (R = Pr, Nd): Nickel valence and the metal-insulator transition investigated by x-ray-absorption spectroscopy. *Phys. Rev. B* **1992**, *46* (23), 14975−14984.
(36) Massa, N. E.; Ramos, A. Y.; Tolentino, H. C. N.; Sousa-Neto, N. M.; Fonseca, J.; Alonso, J. A. Temperature and high-pressure dependent x-ray absorption of $SmNiO_3$ at the Ni K and Sm L_3 edges. *Mater. Res. Express* **2015**, *2* (12), 126301.
(37) Ravel, B.; Newville, M. ATHENA, ARTEMIS, HEPHAESTUS: data analysis for X-ray absorption spectroscopy using IFEFFIT. *J. Synchrotron Radiat.* **2005**, *12* (4), 537−541.
(38) Alonso, J. A.; Martínez-Lope, M. J.; Casais, M. T.; García-Muñoz, J. L.; Fernández-Díaz, M. T.; Aranda, M. A. G. High-temperature structural evolution of $RNiO_3$ (R = Ho, Y, Er, Lu) perovskites: Charge disproportionation and electronic localization. *Phys. Rev. B* **2001**, *64* (9), No. 094102.
(39) Alonso, J. A.; Martínez-Lope, M. J.; Presniakov, I. A.; Sobolev, A. V.; Rusakov, V. S.; Gapochka, A. M.; Demazeau, G.; Fernández-Díaz, M. T. Charge disproportionation in $RNiO_3$ (R = Tm, Yb) perovskites observed in situ by neutron diffraction and ^{57}Fe probe Mossbauer spectroscopy. *Phys. Rev. B* **2013**, *87* (18), 184111.
(40) Alonso, J. A.; García-Muñoz, J. L.; Fernández-Díaz, M. T.; Aranda, M. A. G.; Martínez-Lope, M. J.; Casais, M. T. Charge Disproportionation in $RNiO_3$ Perovskites: Simultaneous Metal-Insulator and Structural Transition in $YNiO_3$. *Phys. Rev. Lett.* **1999**, *82* (19), 3871−3874.
(41) Lacorre, P.; Torrance, J. B.; Pannetier, J.; Nazzal, A. I.; Wang, P. W.; Huang, T. C. Synthesis, crystal structure, and properties of metallic $PrNiO_3$: Comparison with metallic $NdNiO_3$ and semiconducting $SmNiO_3$. *J. Solid State Chem.* **1991**, *91* (2), 225−237.
(42) Granados, X.; Fontcuberta, J.; Obradors, X.; Torrance, J. B. Metastable metallic state and hysteresis below the metal-insulator transition in $PrNiO_3$. *Phys. Rev. B* **1992**, *46* (24), 15683−15688.
(43) Granados, X.; Fontcuberta, J.; Obradors, X.; Mañosa, L.; Torrance, J. B. Metallic state and the metal-insulator transition of $NdNiO_3$. *Phys. Rev. B* **1993**, *48* (16), 11666−11672.
(44) Henry, P. F.; Weller, M. T.; Wilson, C. C. Variable Temperature Powder Neutron Diffraction Study of $SmNiO_3$ through Its M−I Transition Using a Combination of Samarium and Nickel Isotopic Substitution. *Chem. Mater.* **2002**, *14* (10), 4104−4110.
(45) García-Muñoz, J. L.; Aranda, M. A. G.; Alonso, J. A.; Martínez-Lope, M. J. Structure and charge order in the antiferromagnetic band-insulating phase of $NdNiO_3$. *Phys. Rev. B* **2009**, *79* (13), 134432.
(46) Zheng, H.; Zhang, J.; Wang, B.; Phelan, D.; Krogstad, M. J.; Ren, Y.; Phelan, W. A.; Chmaissem, O.; Poudel, B.; Mitchell, J. F. High p_{O2} Floating Zone Crystal Growth of the Perovskite Nickelate $PrNiO_3$. *Crystals* **2019**, *9* (7), 324.
(47) Eiling, A.; Schilling, J. S. Pressure and temperature dependence of electrical resistivity of Pb and Sn from 1−300K and 0−10 GPa-use as continuous resistive pressure monitor accurate over wide temperature range; superconductivity under pressure in Pb, Sn and In. *J. Phys. F: Met. Phys.* **1981**, *11* (3), 623.
(48) Bose, D. N.; Sen, S.; Joshi, D. K.; Vaidya, S. N. Resistivity studies on Ga_2Te_3 and In_2Te_3 under high pressures. *Mater. Lett.* **1982**, *1* (2), 61−63.
(49) Guo, Q.; Magén, C.; Rozenberg, M. J.; Noheda, B. Phenomenological classification of metals based on resistivity. *Phys. Rev. B* **2022**, *106* (8), No. 085141.
(50) Gavriliuk, A. G.; Struzhkin, V. V.; Lyubutin, I. S.; Ovchinnikov, S. G.; Hu, M. Y.; Chow, P. Another mechanism for the insulator-metal transition observed in Mott insulators. *Phys. Rev. B* **2008**, *77* (15), 155112.

https://doi.org/10.1021/acs.jpclett.4c01496
J. Phys. Chem. Lett. 2024, 15, 7716−7723